Synthesis of nano-fibrillated cellulose/magnetite/titanium dioxide (NFC@Fe₃O₄@TNP) nanocomposites and their application in the photocatalytic hydrogen generation

Xingye An[a,b], Dong Cheng[a,b], Lei Dai[b], Baobin Wang[b], Helen Julissa Ocampo[b], Joseph Nasrallah[b], Xu Jia[c], Jijun Zou[c], Yunduo Long[b,**], Yonghao Ni[a,b,*]

[a] Tianjin Key Laboratory of Pulp and Paper, Tianjin University of Science and Technology, Tianjin 300457, China
[b] Department of Chemical Engineering, University of New Brunswick, Fredericton, New Brunswick, E3 B 5A3, Canada
[c] Key Laboratory for Green Chemical Technology of the Ministry of Education, School of Chemical Engineering and Technology, Tianjin University, Tianjin 300072, China

ABSTRACT

Nano-fibrillated cellulose (NFC), an abundant renewable bio-macromolecule, has received much attention in the research community. The study detailed herein is related to the preparation of photocatalytic nanocomposites consisting of nano-fibrillated cellulose/magnetite/titanium dioxide nanoparticles (NFC@Fe₃O₄@TNP). The aim of this study is to improve the photocatalytic efficiency of NFC-TNP composites and to improve their recyclability during the photocatalytic hydrogen generation. The NFC@Fe₃O₄@TNP nanocomposites were characterized by TEM, EDX, SAED, XRD, XPS, FTIR, Raman spectra and VSM techniques. The results showed that Fe₃O₄ NP and TNP were well-distributed on the surface of NFC. The photocatalytic efficiency study showed that NFC@Fe₃O₄@TNP nanocomposites represented a higher photocatalytic hydrogen generation rate in comparison with that of NFC-TNP sample. In addition, the NFC@Fe₃O₄@TNP nanocomposites can be readily recovered from the system using a magnet due to their stable superparamagnetic properties, and they had only a marginal loss of TNP and photocatalytic efficiency after fifteen cycles.

© 2017 Published by Elsevier B.V.

1. Introduction

Nanocellulose, which is a generic term of rod-like or ribbon-like cellulose with a nano-scale dimension, mainly contains nano-fibrillated cellulose (NFC) [1,2], cellulose nano-crystals (CNC) [3] and bacterial cellulose (BC) [4]. NFC, typically produced from cellulosic fibers by mechanical disintegration [5], has generated a great deal of interest as a bio-based nano-sized material due to its sustainable nature, biocompatibility, biodegradability, high specific strength and surface area, among others [6,7].

Among the various applications of NFC, its potential as a support/carrier for catalysts nanoparticles has attracted increased interest in recent years [8]. For instance, Koga et al. applied crystalline cellulose single nanofibers (CSNFs) as a support for gold nanoparticles (Au NP) to obtain CSNFs@AuNP composites, which exhibited an excellent catalytic efficiency (840 times of conventional polymer-supported Au NP) during the reduction of 4-nitrophenol (4-NP) to 4-aminophenol (4-AP) [9]. Additionally, a versatile support/carrier of titanium dioxide nanoparticles (TNP) to prepare NFC-TNP nanocomposites for photocatalytic hydrogen generation was investigated, and the as-prepared nanocomposites showed 2–5 times higher efficiency in comparison with the control TNP [10].

However, two main challenges need to be addressed: first, the cellulose structure of NFC-TNP nanocomposites can be photo-degraded by TNP during photocatalytic hydrogen generation, thus some of the loaded TNP may be lost during the recycling process. Puls et al. [11] and Iguchi et al. [12] also found that TiO₂ can cause the surface pitting/damage of cellulose acetate/cellulose pulp fibers under UV light conditions. Secondly, the photocatalytic efficiency of TiO₂ is limited due to the fast recombination rate of photo-generated electron-hole pairs [13,14].

Magnetite (Fe₃O₄) has been shown to cause no photo-degradation on the cellulose structure during UV irradiation

* Corresponding author at: Department of Chemical Engineering, University of New Brunswick, Fredericton, New Brunswick E3 B 5A3, Canada.
** Corresponding author.
E-mail address: yonghao@unb.ca (Y. Ni).

[15,16]. Additionally, Fe_3O_4 NP were used in numerous applications, such as drug delivery [17], magnetically assisted separation [18] etc., due to their low toxicity, biocompatibility, and superparamagnetic properties [19,20]. Incorporating Fe_3O_4 NP with photocatalysts can be a practical approach to recycle the photocatalysts with an external magnet [20]. Furthermore, the performance of the photocatalysts, such as ZnO [21] and TiO_2 [22], doped with Fe_3O_4, was found to have a higher efficiency than the pristine one. The proposed mechanism was that for Fe_3O_4-based photocatalysts, large amounts of effective electron-trapping sites can be induced by the presence of iron, which would minimize the fast recombination of photo-induced electron-hole pairs, thus improving the photocatalytic efficiency of the Fe_3O_4-based photocatalysts [23–25].

He et al. successfully prepared an innovative $Fe_3O_4@TiO_2$ biomaterial for the treatment of malignant tumors. It was found that the photocatalytic activity of TNP was effectively improved due to the inhibition of the fast recombination of photogenerated electron-hole pairs by Fe_3O_4, and that the recyclability of $Fe_3O_4@TiO_2$ biomaterial was enhanced via an extra magnetic field, compared with the control TiO_2 [26].

In this study, NFC was used as the support/carrier of both Fe_3O_4 NP and TNP to improve the photocatalytic efficiency and recyclability of TNP, and to prepare $NFC@Fe_3O_4@TNP$ nanocomposites for photocatalytic hydrogen generation. TEM, EDX, SAED, XRD, XPS, FTIR, Raman spectra and VSM techniques were carried out to characterize the nanocomposites. Moreover, the photocatalytic efficiency and recyclability of the nanocomposites were also studied.

2. Experimental section

2.1. Materials

Nano-fibrillated cellulose (NFC) (~3.0 wt%) was obtained from Cellulose Lab Co., Ltd. (CAS Number: 9004-34-6). TiO_2 nanoparticles (TNP) powder (mostly anatase, contains a trace amount of rutile) were bought from Shanghai Jianghu Titanium Dioxide Chemical Products Co., Ltd. (China). Hydrochloric acid (HCl, 37%, w/w) and methanol came from Sigma-Aldrich Reagent Co., Ltd. Ferric nitrate nonahydrate ($Fe(NO_3)_3 \cdot 9H_2O$), ferrous sulfate ($FeSO_4 \cdot 7H_2O$), citric acid anhydrous, and sodium hydroxide (NaOH, 50% Soln, w/w) were from Fisher Scientific. All other chemicals were of analytical grade and used without further purification.

2.2. Preparation of Fe_3O_4 nanoparticles

Fe_3O_4 nanoparticles were prepared using chemical co-precipitation of aqueous ferrous and ferric ions as described in the literature [27]. As an example, for the preparation of #1 $NFC@Fe_3O_4$ sample, a diluted HCl solution (20 mL, 2 mol/L) was added to 500 g distilled water, then citric acid (1 mg) was added to the above solution, followed by the additions of 0.44 mol $Fe(NO_3)_3 \cdot 9H_2O$ and 0.22 mol $FeSO_4 \cdot 7H_2O$ solid samples successively with nitrogen bubbling and magnetic stirring (500 rpm). The function of citric acid was to minimize the as-prepared Fe_3O_4 nanoparticles from being oxidized by the dissolving oxygen in water [28]. A diluted NaOH solution (360 mL, 2 mol/L) was added dropwise into the above system, followed by bubbling with nitrogen and magnetic stirring (500 rpm) for 120 min at room temperature to generate Fe_3O_4 nanoparticles. The solid was isolated in the magnetic field and washed three times using distilled water, and the obtained sample was stored for further experiment.

2.3. Preparation of $NFC@Fe_3O_4$ nanocomposites

NFC hydrogel (35 g, ~3 wt%, equivalent to 1 g dried NFC) was diluted to 0.2 wt% with distilled water and stirred for 5 min at 1000 rpm. The diluted NFC suspension was further treated with a sonicator (QSON-ICA) for 3 min to disperse the individual nanocellulose, followed by heating at 65 °C and bubbling with nitrogen for 10 min under magnetic stirring (500 rpm) to remove the dissolved oxygen from NFC suspension. The following procedures for preparation of $NFC@Fe_3O_4$ nanocomposites were similar to those shown in **Part** 2.2. The amounts of citric acid anhydrous, $Fe(NO_3)_3 \cdot 9H_2O$, $FeSO_4 \cdot 7H_2O$ are listed in Table 1. The $NFC@Fe_3O_4$ nanocomposites were obtained via a magnetic field and washed three times with distilled water. The amounts of loaded Fe_3O_4 on the NFC were calculated from Equation (1):

$$M_{Fe_3O_4@NFC} = \frac{M_1 - M_0}{M_0} \tag{1}$$

Where M_0 is the dried mass (g) of blank NFC sample before adsorption of Fe_3O_4 NP; M_1 is the dried mass (g) of $NFC@Fe_3O_4$ nanocomposites after separation. The amounts (mole) of loaded Fe_3O_4 on the surface of NFC were also shown in Table 1. It is noted that not all formed magnetite was loaded onto the NFC, due to the loss in the preparation process, especially at high dosages.

2.4. Preparation of $NFC@Fe_3O_4@TNP$ nanocomposites

TNP suspension was obtained by dispersing 0.2 g of TNP powder in 100 g distilled water, followed by ultrasonic treatment (60% output) for 10 min to disperse the TNP in the aqueous suspension uniformly. The $NFC@Fe_3O_4$ nanocomposites were dispersed into 500 mL distilled water by ultrasonic treatment (60% output) for 15 min and stirring for 5 min at 1000 rpm. Then the TNP suspension was added dropwise into $NFC@Fe_3O_4$ nanocomposites suspension under magnetic stirring at 500 rpm to form well-dispersed $NFC/Fe_3O_4/TNP$/water system, followed by ultrasonic treatment (60% output, 5 min). Further magnetic stirring (500 rpm) for 24 h at ambient temperature was applied to the suspension to ensure good adsorption of TNP on the surface of $NFC@Fe_3O_4$ nanocomposites. The resultant $NFC@Fe_3O_4@TNP$ nanocomposites were obtained in the magnetic field and washed three times with distilled water to remove free TNP. The amount of loaded TNP on the NFC was calculated by Eq. (2):

$$M_{TNPs@NFC} = \frac{M_2 - M_1}{M_0} \tag{2}$$

Where M_0 is dried mass (g) of blank NFC sample before adsorption of TNP; M_1 is dried mass (g) of $NFC@Fe_3O_4$ nanocomposites; and M_2 is dried mass (g) of $NFC@Fe_3O_4@TNP$ nanocomposites after separation.

According Eq. (2) above, the amounts of loaded TNP for $NFC@Fe_3O_4@TNP$ nanocomposites were shown in Table 2.

2.5. Characterization

For the transmission electron microscopy (TEM) analyses, the NFC, TNP powder, $NFC@Fe_3O_4$ nanocomposites and $NFC@Fe_3O_4@TNP$ nanocomposites were individually dispersed into a diluted water suspension before being transferred to a carbon-coated copper grid (about 10 μL by using micropipette) and afterward air-dried at room temperature overnight. The TEM observation was then conducted on a JEOL 2010 transmission electron microscope with 200 kV acceleration voltages. Elemental analyses of energy dispersive X-ray (EDX) and mapping, as well as selected area electron diffraction (SAED) pattern, in combination with TEM were also conducted. The X-ray counts were obtained by integrat-

Table 1
IDs of NFC@Fe$_3$O$_4$ samples and their preparation conditions (the molar ratio of Fe(NO$_3$)$_3$·9H$_2$O to FeSO$_4$·7H$_2$O was 2, the function of citric acid was to minimize the formed magnetite from being oxidized).

Sample ID	Fe(NO$_3$)$_3$·9H$_2$O (mmol)	FeSO$_4$·7H$_2$O (mmol)	Citric acid (mg)	Loaded Fe$_3$O$_4$ (mmol)
#1 NFC@Fe$_3$O$_4$	0.44	0.22	1.0	0.21
#2 NFC@Fe$_3$O$_4$	0.88	0.44	2.0	0.41
#3 NFC@Fe$_3$O$_4$	1.76	0.88	4.0	0.82
#4 NFC@Fe$_3$O$_4$	2.64	1.32	6.0	1.21
#5 NFC@Fe$_3$O$_4$	4.40	2.20	10.0	2.00
#6 NFC@Fe$_3$O$_4$	6.16	3.08	14.0	2.57
#7 NFC@Fe$_3$O$_4$	8.80	4.40	20.0	3.11
#8 NFC@Fe$_3$O$_4$	10.47	5.24	24.0	3.61
#9 NFC@Fe$_3$O$_4$	13.10	6.55	30.0	4.21

Table 2
IDs of NFC@Fe$_3$O$_4$@TNP samples and their loaded amounts of Fe$_3$O$_4$ and TNP, and the molar ratio.

Sample ID	Loaded Fe$_3$O$_4$ (mmol)	Loaded TNP (mg)	Loaded TNP (mmol)	Fe$_3$O$_4$/TNP (mmol/mmol)
#1 NFC@Fe$_3$O$_4$@TNP	0.21	184.2	2.31	0.09
#2 NFC@Fe$_3$O$_4$@TNP	0.41	179.8	2.25	0.18
#3 NFC@Fe$_3$O$_4$@TNP	0.82	175.9	2.20	0.37
#4 NFC@Fe$_3$O$_4$@TNP	1.21	169.5	2.12	0.57
#5 NFC@Fe$_3$O$_4$@TNP	2.00	159.4	2.00	1.00
#6 NFC@Fe$_3$O$_4$@TNP	2.57	139.6	1.75	1.47
#7 NFC@Fe$_3$O$_4$@TNP	3.11	99.7	1.25	2.45
#8 NFC@Fe$_3$O$_4$@TNP	3.61	85.2	1.07	3.37
#9 NFC@Fe$_3$O$_4$@TNP	4.21	69.3	0.87	4.84

ing Kα X-ray peaks using an EDAX PV 9900 EDX microanalyser [29]. The phase structure of the NFC (dried), TNP powder, Fe$_3$O$_4$ powder, NFC@Fe$_3$O$_4$ nanocomposites (dried) and NFC@Fe$_3$O$_4$@TNP nanocomposites (dried) were analyzed using an X-ray powder diffractometer (XRD, Bruker D8 Advance Spectrometer). The X-ray source was a sealed, 2.2 kW Cu X-ray tube, maintained at an operating current of 40 kV and 30 mA. A 2θ Bragg angle between 10° and 80°, step size of 0.02°, and a step time of 1.0 s were used during the measurements [30]. The chemical binding energies of the respective ions in the samples were measured using X-ray photoelectron spectroscopy (XPS, ESCALa-b220i-XL electron spectrometer, ThermoFisher Scientific K-Alpha, UK) under 300 W Al Kα radiation. Fourier transform infrared spectroscopy (FTIR) spectra of NFC, TNP powder, Fe$_3$O$_4$ powder, NFC@Fe$_3$O$_4$ nanocomposites and NFC@Fe$_3$O$_4$@TNP nanocomposites were taken on a KBr disk in the frequency range of 4000–400 cm^{-1} by using a FTIR spectrophotometer (Spectrum 100). Raman spectra were recorded on a laser micro-Raman spectrometer (LabRAM HR Evolution) with the exciting wavelength at 532 nm [31]. The magnetic properties were measured with a vibrating sample magnetometer (VSM), physical property measurement system, at 25 °C as a function of the applied magnetic field between −100 and 100 kOe.

2.6. Photocatalytic hydrogen generation

The photocatalytic hydrogen generation experiments were carried out at room temperature under an atmospheric pressure in a closed quartz reactor system as shown in Fig. 1. A 300 W Xe lamp (about 300 nm of wavelength) was used as the light source. NFC@Fe$_3$O$_4$@TNP nanocomposites were dispersed in an aqueous solution containing 95 mL H$_2$O and 25 mL methanol (20 vol%, acted as a sacrificial hole acceptor), and subjected to UV irradiation, by following similar experimental set-up detailed in the literature [32]. The amount of hydrogen generated was collected and analyzed by a thermal conductivity detector (TCD) gas chromatograph (China, GC-9200, MS-5A zeolite column, argon as the carrier gas) [33].

2.7. Recyclability of NFC@Fe$_3$O$_4$@TNP nanocomposites

The recyclability experiments were conducted as follows: the NFC@Fe$_3$O$_4$@TNP nanocomposites were collected and enriched by a magnet and washed with distilled water for three times. The wet NFC@Fe$_3$O$_4$@TNP sample was then collected, and a small amount of nanocomposites was taken for determining the moisture content. Then the wet NFC@Fe$_3$O$_4$@TNP nanocomposites collected were reused for the next run, and small amounts of make-up nanocomposites were also added to the new run to compensate for those that were taken for moisture determination, together with the small loss.

3. Results and discussion

3.1. Concept of NFC@Fe$_3$O$_4$@TNP nanocomposites preparation for improving their photocatalytic efficiency and recyclability

Fig. 1 illustrates the concept of synthesizing the NFC@Fe$_3$O$_4$@TNP nanocomposites, the photocatalytic hydrogen generation process, as well as the recycling of NFC@Fe$_3$O$_4$@TNP nanocomposites by a magnet. NFC with a width of 60–100 nm are shown in Fig. 1(a). Fig. 1(b) shows the in-situ preparation of Fe$_3$O$_4$ NP (5–8 nm) and then immobilization on the surface of NFC (Fig. 1(c)) to form the NFC@Fe$_3$O$_4$ nanocomposites. Fig. 1(d) and (e) show that TNP (ca. 10 nm) were loaded uniformly onto the surface of NFC@Fe$_3$O$_4$ nanocomposites through sonification and mechanical stirring, to form NFC@Fe$_3$O$_4$@TNP nanocomposites. The as-prepared NFC@Fe$_3$O$_4$@TNP nanocomposites were then subjected to UV irradiation for photocatalytic hydrogen generation. The magnetic separation technique was applied to recycle the nanocomposites for the next run.

The proposed concept was based on:

1) NFC can be an efficient support/carrier for both Fe$_3$O$_4$ NP and TNP to fabricate NFC@Fe$_3$O$_4$@TNP nanocomposites, while the original properties of the nanoparticles can be maintained.
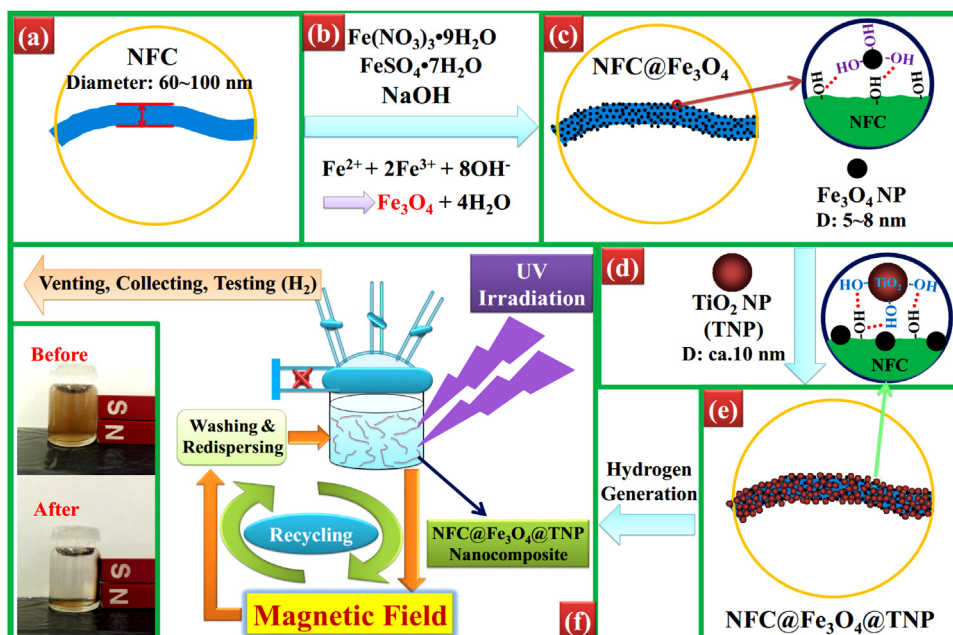
Fig. 1. Schematic representation for the preparation of NFC@Fe$_3$O$_4$@TNP nanocomposites for photocatalytic hydrogen generation and recyclability; (a) NFC, (b) in-situ preparation of Fe$_3$O$_4$ NP, (c) loaded Fe$_3$O$_4$ NP on the surface of NFC with hydrogen bonds, (d) adding dispersed TNP into as-prepared NFC@Fe$_3$O$_4$ nanocomposites suspension, (e) loaded TNP on the surface of NFC@Fe$_3$O$_4$ nanocomposites by hydrogen bonding with NFC and (f) schematic of photocatalytic hydrogen generation and recyclability of NFC@Fe$_3$O$_4$@TNP nanocomposites.

2) The physical coating layers/increased electron-trapping sites from Fe$_3$O$_4$ NP could minimize the photo-degradation of NFC under UV irradiation, thus improving the stability and recyclability of NFC@Fe$_3$O$_4$@TNP nanocomposites.

3) The photocatalytic efficiency of TNP can be improved through the Fe$_3$O$_4$ NP induced inhibition of fast recombination of photo-generated electron-hole pairs.

4) NFC@Fe$_3$O$_4$@TNP nanocomposites can be readily recycled via a magnet.

3.2. Characterization of NFC@Fe$_3$O$_4$@TNP nanocomposites

3.2.1. TEM analyses

The morphology of NFC is shown in Fig. 2(a), it is noted that NFC has a width of about 60–80 nm and a length of several micrometers. Compared with the pristine NFC, the NFC@Fe$_3$O$_4$ nanocomposites (Fig. 2(b) and (c)) confirm that Fe$_3$O$_4$ NP (5–8 nm) via the in-situ method, were prepared on the surface of NFC. EDX spectra of the NFC@Fe$_3$O$_4$ nanocomposites (Fig. 2(d)) support the existence of Fe$_3$O$_4$ NP in the NFC@Fe$_3$O$_4$ nanocomposites. The SAED patterns shown in Fig. 2(e) indicate the crystalline nature of the Fe$_3$O$_4$ nanoparticles.

A single #4 NFC@Fe$_3$O$_4$@TNP sample is shown in Fig. 3(a) and (b). Both Fe$_3$O$_4$ NP and TNP were uniformly loaded on the surface of NFC. In addition, EDX spectra of NFC@Fe$_3$O$_4$@TNP nanocomposites (Fig. 3(c)) support the existence of Fe$_3$O$_4$ NP and TNP, and their SAED patterns (Fig. 3(d) and (e)) indicate that the loaded Fe$_3$O$_4$ NP and TNP on the surface of NFC maintained their original crystalline nature. The results of EDX element mappings (Fe and Ti) of NFC@Fe$_3$O$_4$@TNP nanocomposites (Fig. 3(f)–(i)) confirm that Fe (red, Fig. 3(g)) and Ti (green, Fig. 3(h)) were rather evenly distributed in the NFC@Fe$_3$O$_4$@TNP nanocomposites. Images of Fe$_3$O$_4$ NP and TNP (Fig. 3(g) and (h)) were overlapped with the same in Fig. 3(j), which further confirms that both Fe$_3$O$_4$ NP and TNP were well-distributed on the surface of NFC.

3.2.2. XRD analyses

As shown in Fig. 4(a), (d) and (e), the XRD patterns of NFC, NFC@Fe$_3$O$_4$ and NFC@Fe$_3$O$_4$@TNP nanocomposites contained three characteristic peaks at $2\theta = 14.8°$ (101), 16.4° (10$\bar{1}$) and 22.5° (002), which are attributed to cellulose I [34]. The characteristic peaks of as-prepared Fe$_3$O$_4$ NPs of 30.1°, 35.6°, 43.4, 54.0°, 57.0°, and 62.7°, which are attributed to their (220), (311), (400), (422), (511), and (440) crystal planes, respectively [20,35], were evident in Fig. 4(c) and (d). The as-prepared Fe$_3$O$_4$ XRD pattern (Fig. 4(c)) also had the diffraction peaks that can be indexed to cubic phase spinel Fe$_3$O$_4$ [36], which can also be found in the diffraction peaks of NFC@Fe$_3$O$_4$ (Fig. 4(d)). These results confirmed that the loaded Fe$_3$O$_4$ NP on the surface of NFC maintained their cubic spinel crystal phase properties.

The characteristic peaks of TNP (anatase) are shown in Fig. 4(b) and (e): 25.3°, 37.8°, 48.0°, 54.0°, 55.1°, 62.7°, 68.8°, 70.3° and 75.1°, which are related to the (101), (004), (200), (105), (211), (204), (116), (220) and (215) crystal planes, respectively [37]. The results above support the conclusion that the original properties of Fe$_3$O$_4$ NP and TNP, such as, crystal structures, superparamagnetic properties and photocatalytic activity, maintained the same after they were loaded onto NFC surface.

Sun et al. used BCN as carrier of both Pd and Cu NP by an in-situ precipitation method. It was found that the Pd and Cu nanoparticles were well dispersed/loaded on the surface of BCN, and that the original XRD patterns of Pd and Cu NP were maintained in these composites, which guaranteed the Pd-Cu/BCN composites as catalysts for water de-nitrification with a high catalytic activity [38].

3.2.3. XPS analyses

As shown in Fig. 5(a), the peaks at around 460 eV were due to the Ti^{4+} element, and the core level photoelectron spectra of Ti2p (inserted image in Fig. 5(a)) exhibited two different signals of Ti2p$_{3/2}$ and Ti2p$_{1/2}$ at 458.4 eV and 464.2 eV, respectively. The above results were consistent with those in the literature [39]. The XPS results of Fe$_3$O$_4$ NP (Fig. 5(b)), showed that the typical XPS
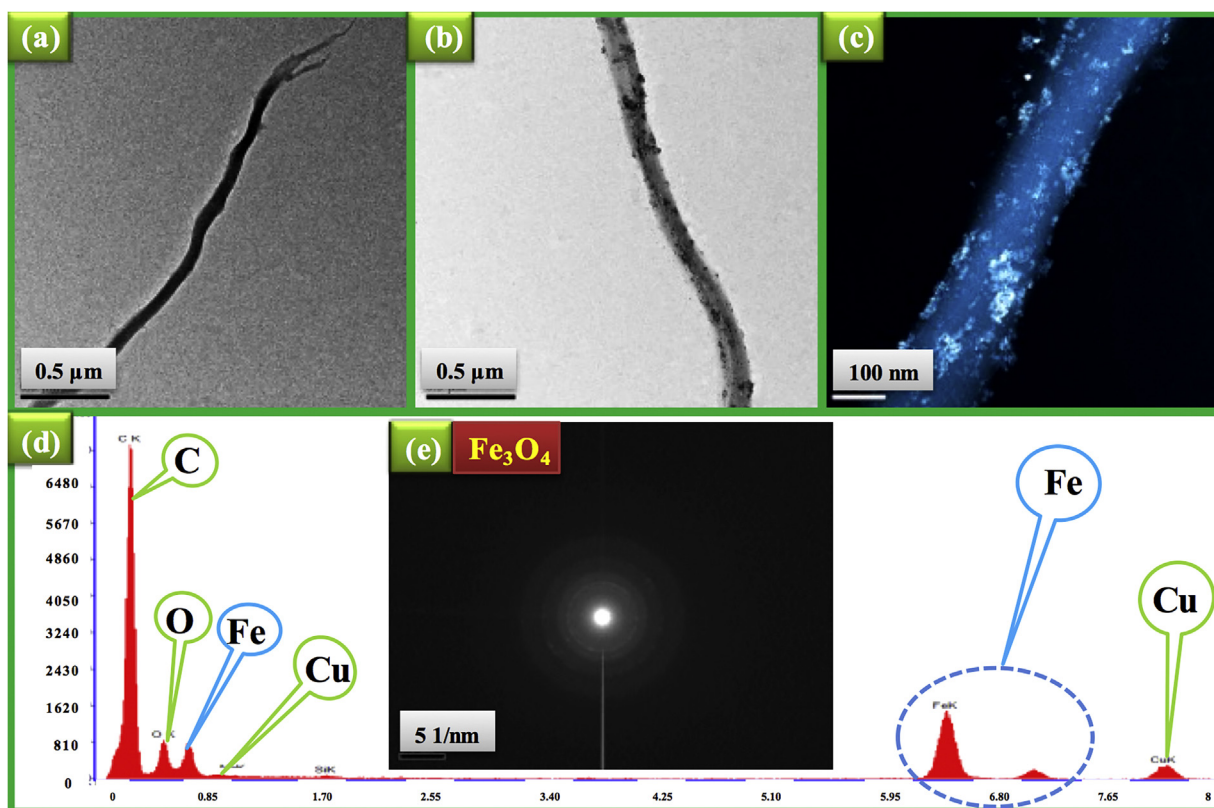
Fig. 2. TEM images of (a) NFC, (b) and (c) #4 NFC@Fe$_3$O$_4$ nanocomposites, (d) corresponding EDX spectra of #4 NFC@Fe$_3$O$_4$ nanocomposites, (Scale bars of (a) 0.5 μm, (b) 0.5 μm and (c) 100 nm) (e) Fe$_3$O$_4$ NP SAED patterns.
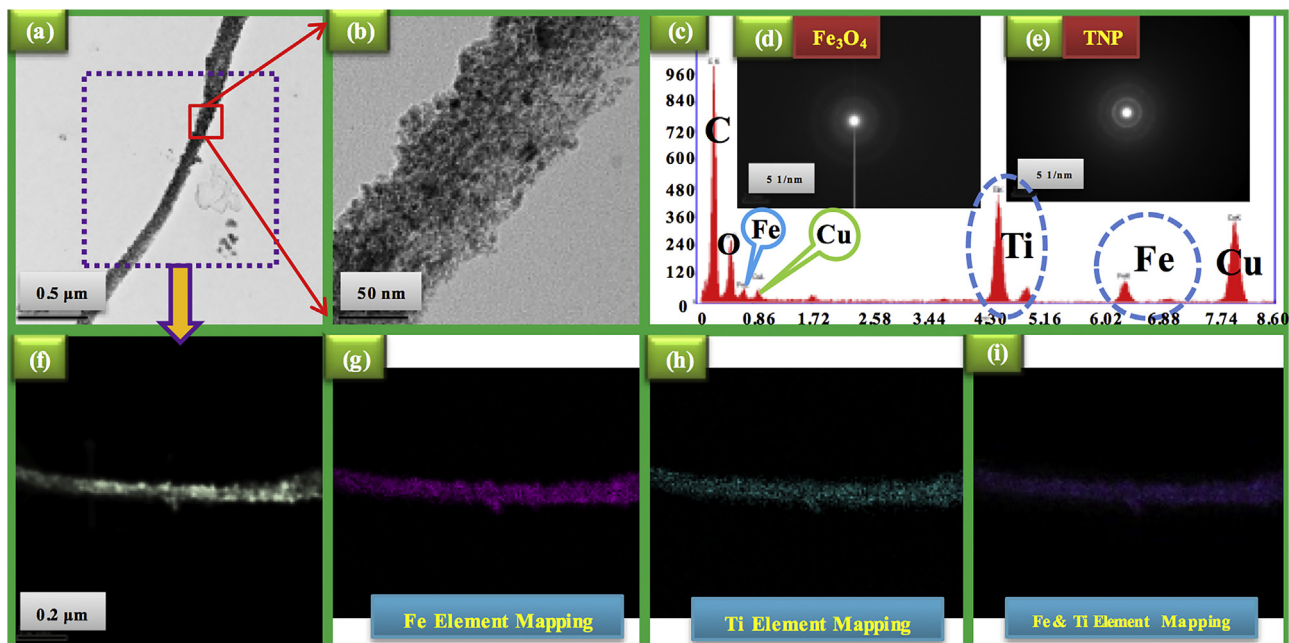

Fig. 3. TEM images of (a) #4 NFC@Fe$_3$O$_4$@TNP nanocomposites, (b) magnified region as indicated in (a), (f) scanning bright field image (rotating 90° from the indicated region in (a)), (Scale bars of (a) 0.5 μm, (b) 50 nm and (f) 0.2 μm), (c) corresponding EDX spectra of #4 NFC@Fe$_3$O$_4$@TNP nanocomposites, (d) Fe$_3$O$_4$ NP SAED patterns, (e) TNP SAED patterns, (g) corresponding Fe element mapping of (f), (h) corresponding Ti element mapping of (f), (i) Fe & Ti element overlapped mapping of (g) and (h).

spectra of Fe2p were at between 700–740 eV, and the core level photoelectron spectra of Fe2p (inserted image in Fig. 5(b)) exhibited two different signals of Fe2p$_{3/2}$ and Fe2p$_{1/2}$ at 710.9 eV and 725.1 eV, respectively, which were reported by others [40].

The XPS spectrum of NFC@Fe$_3$O$_4$ nanocomposites is shown in Fig. 5(c), the main peaks were C1s, O1s and Fe2p centered at around 285 eV, 530 eV and 720 eV, respectively.

The Fe2p$_{3/2}$ and Fe2p$_{1/2}$ binding energies (inserted image of Fig. 5(c)) for NFC@Fe$_3$O$_4$ nanocomposites were 710.6 eV and
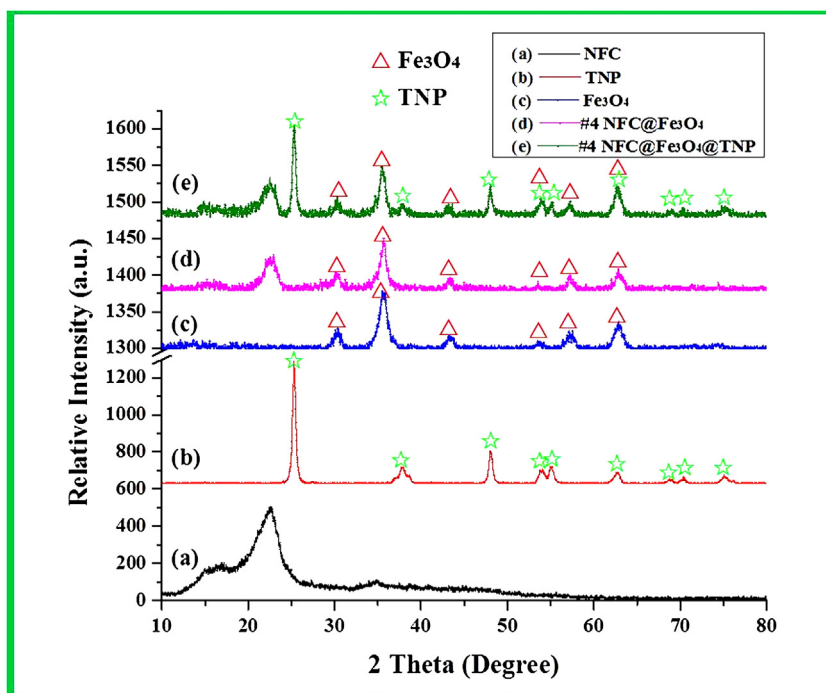
Fig. 4. XRD spectra of: (a) NFC; (b) TNP; (c) Fe$_3$O$_4$; (d) #4 NFC@Fe$_3$O$_4$ nanocomposites; (e) #4 NFC@Fe$_3$O$_4$@TNP nanocomposites. The XRD spectra of (d) NFC@Fe$_3$O$_4$ nanocomposites included typical peaks of both (a) NFC and (c) Fe$_3$O$_4$; while the XRD spectrum of (e) NFC@Fe$_3$O$_4$@TNP nanocomposites contained characteristic peaks of (a) NFC, (b) TNP and (c) Fe$_3$O$_4$.

725.3 eV, respectively, which was in good agreement with the results of Fig. 5(b), indicated the presence of Fe$_3$O$_4$ in nanocomposites [41]. As for the XPS spectrum of NFC@Fe$_3$O$_4$@TNP nanocomposites shown in Fig. 5(c), the main peaks were C1s, Ti2p, O1s and Fe2p centered at around 285 eV, 460 eV, 530 eV and 720 eV, respectively, which corresponded with the results of Fig. 5(a) and (b), indicated the presence of Fe$_3$O$_4$ and TNP in the nanocomposites [36]. The core level photoelectron spectra of Ti2p and Fe2p shown in the inserted images of Fig. 5(d) had same binding energies compared with those of Fig. 5(a) and (b), which further confirmed that TNP and Fe$_3$O$_4$ were presented in the final nanocomposites and that the original properties of Fe$_3$O$_4$ NP and TNP, such as, phase structures, superparamagnetic property and photocatalytic activity, maintained the same after they were loaded onto NFC surface.

3.2.4. FTIR analyses

FTIR spectra of NFC, TNP, Fe$_3$O$_4$, #4 NFC@Fe$_3$O$_4$ and #4 NFC@Fe$_3$O$_4$@TNP nanocomposites are shown in Fig. 6. The peaks at 1646 cm^{-1} of all the samples were due to the H—O—H stretching vibration of absorbed water [42]. As for TNP and Fe$_3$O$_4$ (Fig. 6(b) and (c)), the broad bands in the 3740–3300 cm^{-1} regions (marked as shaded area (2)) were ascribed to O—H stretching vibrations, which indicated that there were a large amount of hydroxyl groups on the surface of nanoparticles [43]. The Ti—O—Ti bonds of TNP can be observed by the presence of wide bands below 800 cm^{-1} [44], which is shown in Fig. 6(b), while the characteristic band of Fe$_3$O$_4$ appeared at around 600 cm^{-1} [45], as shown in Fig. 6(c).

The FTIR results may show some evidence regarding the hydrogen bonds between NFC and Fe$_3$O$_4$ or TNP. The hydroxyl groups of NFC have characteristic vibrations at 3352 cm^{-1} (Fig. 6(a)), similar to those reported in the literature [3]. For the NFC@Fe$_3$O$_4$ and NFC@Fe$_3$O$_4$@TNP samples, the corresponding hydroxyl groups peaked at 3330 cm^{-1} (Fig. 6(d)) and 3319 cm^{-1} (Fig. 6(e)), respectively. These small shifts may be due to the interactions between the hydroxyl groups of NFC and Fe$_3$O$_4$ or TNP through hydrogen bonds. It should be pointed out that other mechanisms, such as van

der Vaals forces, may also play a role for the interactions between NFC and nanoparticles.

3.2.5. Raman spectra analyses

As shown in Fig. 7(a), the Raman spectra of NFC exhibited characteristic peaks of cellulose at the range of 300–1500 cm^{-1} [46]. The Raman spectra of TNP in Fig. 7(b), clearly shows that the spectrum of TNP has four typical peaks (at 157, 404, 517, and 640 cm^{-1}), which demonstrated that the TNP is mainly constituted by anatase [47]. As for the Raman spectra of Fe$_3$O$_4$ shown in Fig. 7(c), the characteristic peaks of Fe$_3$O$_4$ at 331, 524 and 670 cm^{-1} confirmed that the as-synthesized Fe$_3$O$_4$ NP were composed of the magnetite phase [48].

It can be noted that the Raman spectra of NFC@Fe$_3$O$_4$ nanocomposites (Fig. 7(d)) contained all the typical peaks of NFC and Fe$_3$O$_4$, which verified the existence of Fe$_3$O$_4$ in the NFC@Fe$_3$O$_4$ nanocomposites. Similarly, the Raman spectra of NFC@Fe$_3$O$_4$@TNP nanocomposites contained all the typical peaks of NFC, Fe$_3$O$_4$ and TNP, which identified the presence of Fe$_3$O$_4$ and TNP in the NFC@Fe$_3$O$_4$@TNP nanocomposites. The Raman spectra results were corresponding with those of FTIR analyses.

3.3. Photocatalytic hydrogen generation activity

Fig. 8 presents the photocatalytic hydrogen generation efficiency over the NFC NFC@Fe$_3$O$_4$@TNP nanocomposites with different molar ratios of Fe$_3$O$_4$/TNP, compared with those of the control TNP, NFC@TNP and NFC@Fe$_3$O$_4$ samples. It can be seen from Fig. 8(a-1) that with the increase of mole amount of Fe$_3$O$_4$ loading onto the NFC surface (from 0.21 to 4.21 mmol), the amount of TNP loading on the same NFC sample decreased from 2.31 to 0.87 mmol. The above can be explained by the limited surface area of NFC. As shown in Fig. 8(b), it was found that the rate of hydrogen generation of #1–#9 NFC@Fe$_3$O$_4$@TNP nanocomposites was 4.62–8.23 times higher than that of the control TNP (53 μmol/(min gTNP)). NFC@Fe$_3$O$_4$ nanocomposites (without TNP)
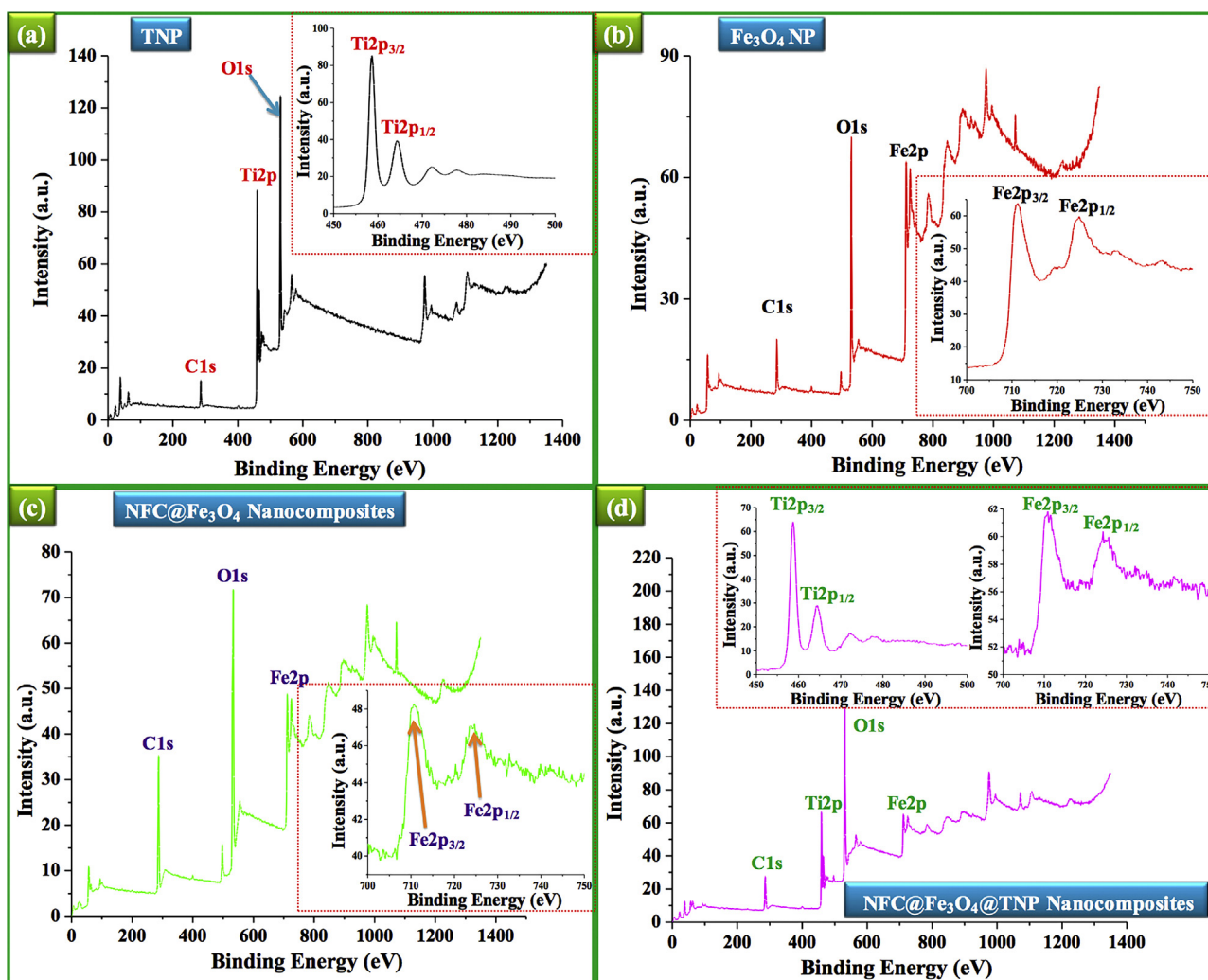
Fig. 5. XPS survey scan of the surface of (a) TNP, (b) Fe_3O_4 NP, (c) #4 NFC@Fe_3O_4 nanocomposites and (d) #4 NFC@Fe_3O_4@TNP nanocomposites; the typical Fe2p and Ti2p peaks corresponding to the Fe_3O_4 NP and TNP were shown in the XPS patterns, which indicated the existence of Fe_3O_4 and TNP in the nanocomposites.

cannot generate hydrogen under otherwise the same condition (Fig. 8(b)).

As shown in Fig. 8(a) and (a-2), the amounts of hydrogen generation for Samples #1–#3 increased from 3306 to 4018 μmol as the molar ratio of Fe_3O_4/TNP increased from 0.09 to 0.37, then decreased to 850 μmol for Sample #9 as the molar ratio of Fe_3O_4/TNP increased to 4.84. The hydrogen generation rates (Fig. 8(b)) for Samples #1–#7 increased from 299 to 436 μmol/(min·gTNP) as the molar ratio of Fe_3O_4/TNP increased from 0.09 to 2.45, then decreased to 245 μmol/(min gTNP) for Sample #9 as the molar ratio of Fe_3O_4/TNP increased to 4.84.

The above results can be explained as follows: the existence of low amount of Fe_3O_4 NP on the surface of NFC (Fe_3O_4/TNP was from 0.09 to 0.37) increased the electron-trapping sites, thus prohibiting the fast recombination of photo-induced electron-hole pairs, consequently improving the photocatalytic efficiency of TNP.

However, in the high Fe_3O_4/TNP molar ratio (Sample #8 and #9), two main reasons can be ascribed to the reduced photocatalytic efficiency of hydrogen generation: 1) the excessive Fe_3O_4 NP loading onto the limited NFC surface would cause aggregation of Fe_3O_4, thus covering part of the loaded TNP, rendering them less efficient during the photocatalytic hydrogen generation process; 2) excessive Fe_3O_4 would produce too many electron-trapping sites, thus decreasing the amount of effective photo-induced electrons for hydrogen generation.

Similar results were reported in the literature. For instance, Harifi and Montazer synthesized a magnetically separable Fe_3O_4 loaded TiO_2 nanocomposites for dye photo-degradation through a novel simple strategy, and found that the photo-degradation efficiency (rate constant k) for Methylene Blue of the prepared Fe_3O_4-TiO_2 nanocomposites increased from 0.67 to 1.13 h^{-1}, as the low molar ratio of Fe_3O_4/TiO_2 increased from 0.16 to 0.41, and that the photo-degradation efficiency decreased to 0.53 h^{-1} when the molar ratio of Fe_3O_4/TiO_2 increased to 0.80 [49].

Ma et al. prepared Fe_3O_4-TiO_2 nanosheets (Fe_3O_4-TNS) by means of lamellar reverse micelles and solvothermal method, and found that Fe_3O_4-TNS nanosheets exhibited better photocatalytic antibacterial activity toward Gram-negative *Escherichia coli* and Gram-positive *Staphylococcus aureus* than pure TiO_2. The less recombination and more efficient separation of photo-induced electro-hole pairs in the Fe_3O_4-TNS composites were credited [40].

### 3.4. Recyclability and magnetic properties of NFC@Fe_3O_4@TNP nanocomposites

The recyclability testing of NFC@Fe_3O_4@TNP nanocomposites for photocatalytic hydrogen generation was carried out, as shown in Fig. 9. The photocatalytic nanocomposites were recovered by a magnet after each cycle (Fig. 9(c) and (d)). The amount of generated hydrogen had a marginal loss after fifteen cycles, and
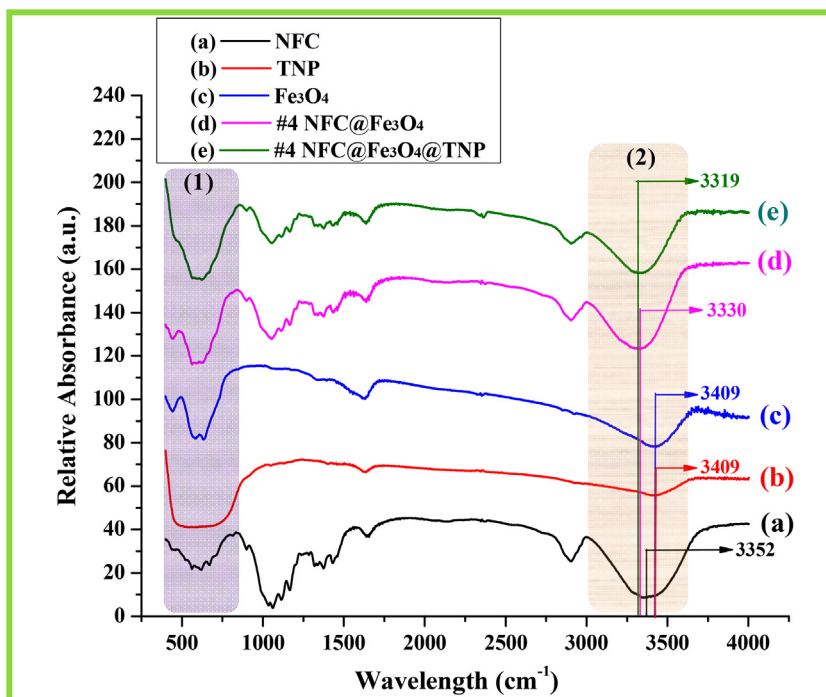
Fig. 6. FTIR spectra of (a) NFC, (b)TNP, (c) Fe_3O_4 NP, (d) #4 NFC@Fe_3O_4 nanocomposites and (e) #4 NFC@Fe_3O_4@TNP nanocomposites; the marked area shown in the patterns indicated the existence of Fe_3O_4 and TNP in the nanocomposites.
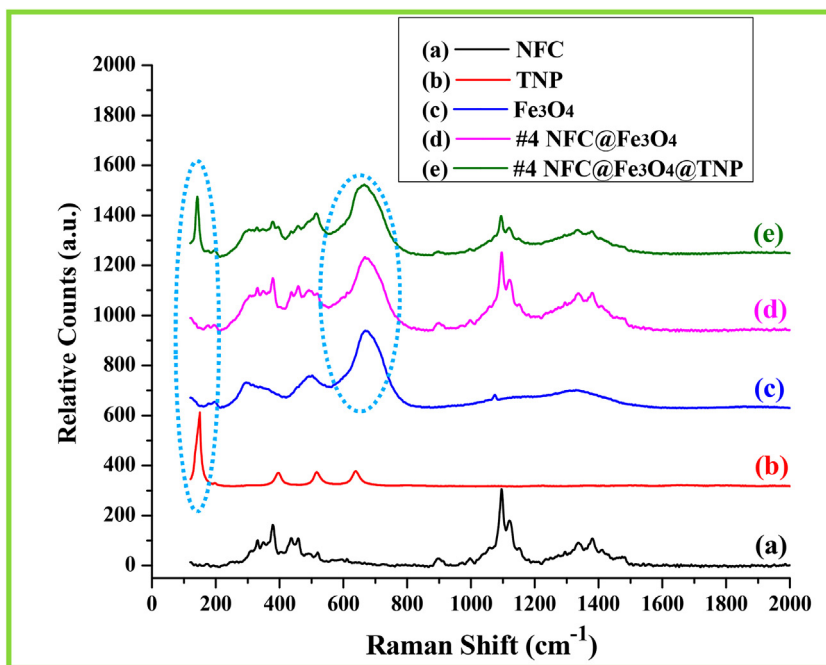
Fig. 7. Raman spectra of (a) NFC, (b) TNP, (c) Fe_3O_4 NP, (d) #4 NFC@Fe_3O_4 nanocomposites and (e) #4 NFC@Fe_3O_4@TNP nanocomposites; the marked area shown in the patterns indicated the existence of Fe_3O_4 and TNP in the NFC@Fe_3O_4@TNP nanocomposites.

the photocatalytic efficiency decreased only slightly (from 395 to 365 μmol/(min gTNP)), which indicated the high stability and excellent recyclability of NFC@Fe_3O_4@TNP nanocomposites under the reaction conditions studied.

There are two main reasons for the results above: 1) superparamagnetic property of Fe_3O_4 NPs warranted the recyclability of NFC@Fe_3O_4@TNP nanocomposites; 2) the protect effect of the loaded Fe_3O_4 for NFC can maintain the high stability of NFC@Fe_3O_4@TNP nanocomposites.

There could be three fundamental reasons below for the protecting effects of Fe_3O_4 on NFC:

1) Fe_3O_4 NP can function as a physical coating layer onto the NFC surface, thus protecting NFC from photo-degradation by TiO_2, as supported by the TEM results (Fig. 3(a) and (b)). Similar observation was made in the literature. For example, Ren et al. anchored Fe_3O_4 nanoparticles onto helical carbon nanofibers to prepare high-performance anodes in lithium-ion batteries, and found
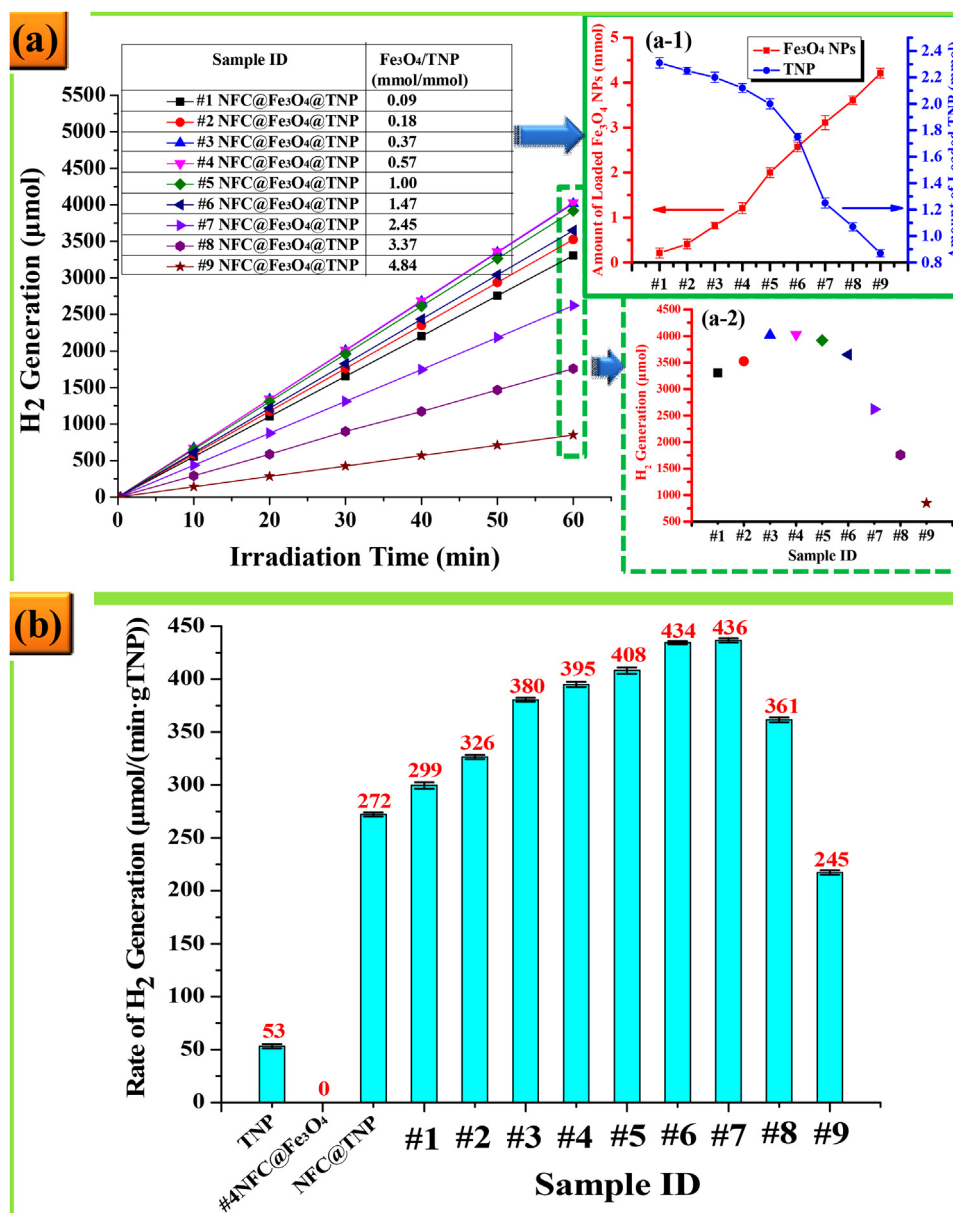
Fig. 8. (a) Photocatalytic hydrogen generation as a function of irradiation time for NFC@Fe$_3$O$_4$@TNP nanocomposites under UV light irradiation, the mole amounts of loaded Fe$_3$O$_4$ NP and TNP were shown in Fig. 8(a-1), those during the H$_2$ generation were shown in Fig. 8(a-2); (b) rates of hydrogen generation from different samples (Reaction condition: 20 °C, 300 W Xe lamp (about 300 nm of wavelength), 60 min, reaction solution containing 95 mL H$_2$O and 25 mL methanol (20 vol%)).

that the Fe$_3$O$_4$-anchored carbon nanofiber composites exhibited a much better stability and cyclic stability and rate capability compared with the non-anchored nanofiber [50].

2) Fe$_3$O$_4$ NP coating may act as a shield on the surface of NFC, thus preventing NFC from UV light degradation directly (UV-blocking agent). Mirjalili prepared a cotton fabric with special functions by coating graphene oxide and Fe$_3$O$_4$ nanoparticles accomplished in one step, and found that the nanocomposite treated cotton fabric had much lower UV transmittance compared to the raw cotton fabric [51].

3) The increased electron-trapping sites from Fe$_3$O$_4$ NP may decrease the photo-gradation of NFC, partially contributing to the increased stability of photocatalysts; other mechanisms that have not yet been identified, may also be possible.

Many investigations have shown that the loaded Fe$_3$O$_4$ in the composites possessed desirable superparamagnetic properties that

guaranteed the excellent recyclability of nanocomposites. Abbas et al. synthesized Fe$_3$O$_4$/TiO$_2$ core/shell nanotubes to remove the methylene blue (MB) from waste water by photocatalytic reaction, and found that the as-prepared composites performed about 90% removal of MB even after a six-cycle run by magnetic separation [24]. Mahmoud et al. prepared CNC/Fe$_3$O$_4$ NP/Au NP nanocomposites for efficient immobilization of papain enzyme and found that the CNC/Fe$_3$O$_4$ NP/Au NP/papain composites retained more than 80% of their initial activity after 12 cycles of magnetic separation [52].

In fact, we have experimentally determined the amounts of NFC@Fe$_3$O$_4$@TNP nanocomposites after each cycle and found that the loss of nanocomposites for each cycle was very small (Fig. S2). These results further indicate the high stability of these NFC@Fe$_3$O$_4$@TNP nanocomposites during the recycling process.

Fig. 10(a) shows the magnetic properties of Fe$_3$O$_4$ NP, NFC@Fe$_3$O$_4$ nanocomposites and NFC@Fe$_3$O$_4$@TNP nanocompos-
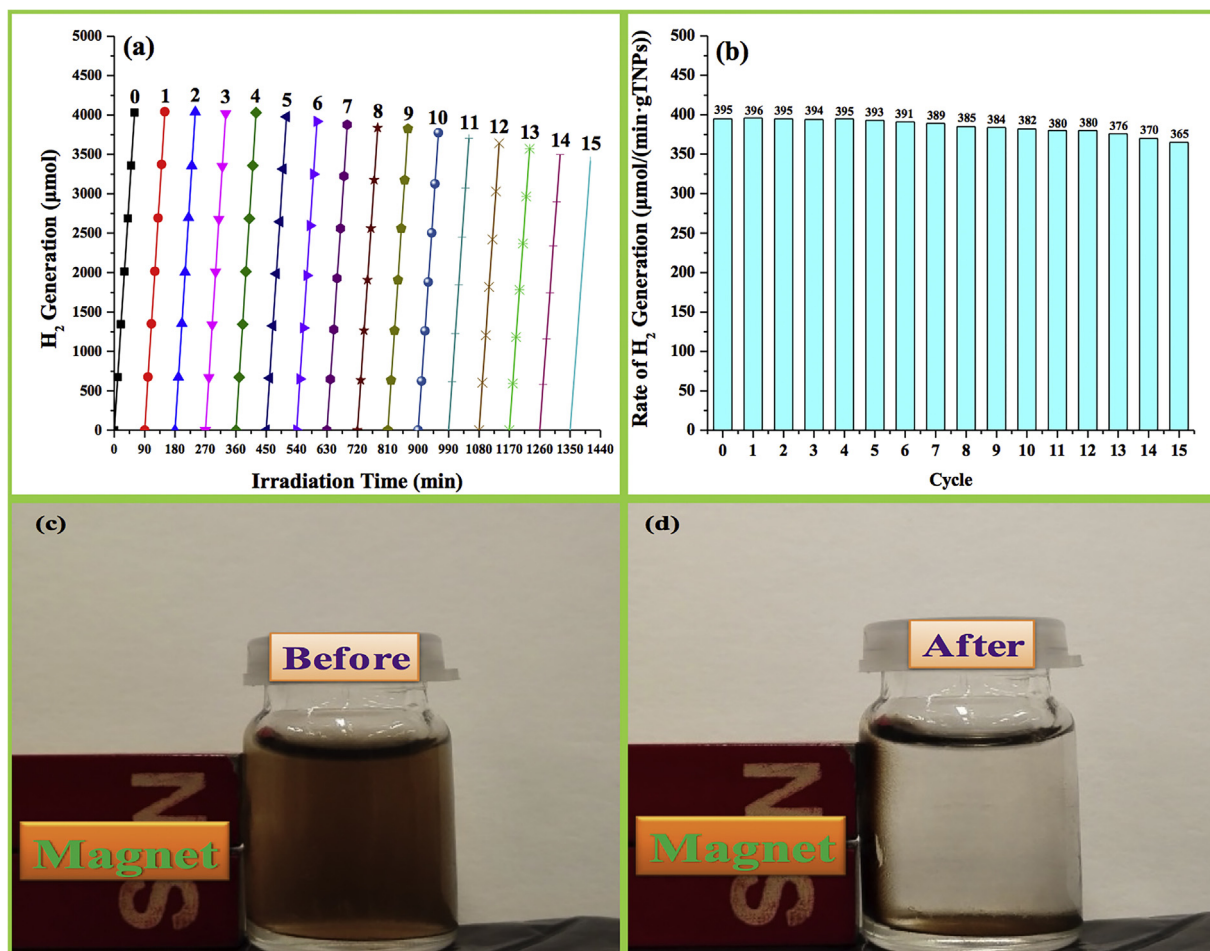
Fig. 9. Recyclability of #4 NFC@Fe$_3$O$_4$@TNPs nanocomposites: (a) cycling tests of photocatalytic hydrogen generation, (b) the corresponding rate of H$_2$ generation, as well as photographs of #4 NFC@Fe$_3$O$_4$@TNP nanocomposite suspension (c) before, and (d) after an external magnetic field was applied. (Reaction condition: 20 °C, 300 W Xe lamp (about 300 nm wavelength), 60 min, reaction solution containing 95 mL H$_2$O and 25 mL methanol (20 vol%)).
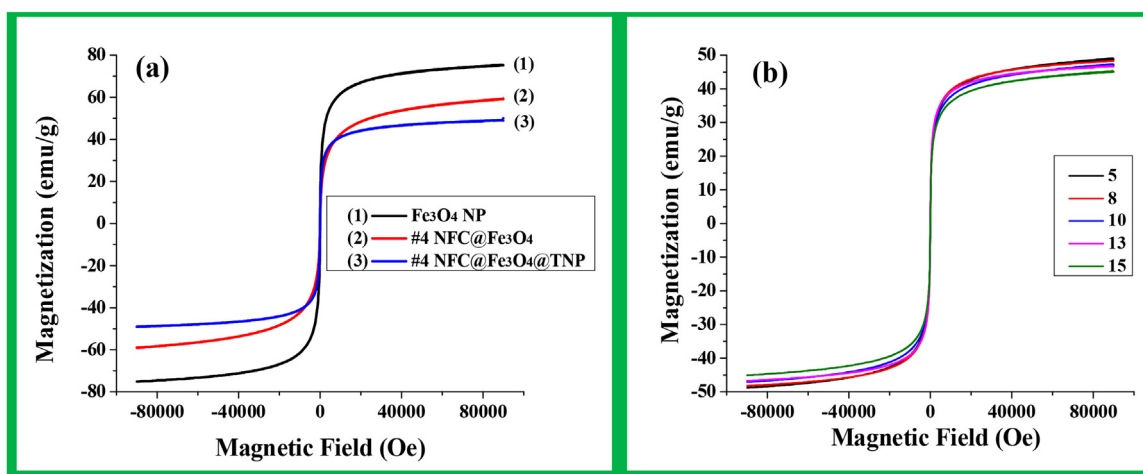
Fig. 10. Magnetization curves of the Fe$_3$O$_4$ NP, #4 NFC@Fe$_3$O$_4$ nanocomposites, #4 NFC@Fe$_3$O$_4$@TNP nanocomposites (a), as well as #4 NFC@Fe$_3$O$_4$@TNP nanocomposites from different cycles.

ites. The saturation magnetization for the Fe$_3$O$_4$ NP is 75 emu/g, and it decreases to 60 emu/g for NFC@Fe$_3$O$_4$ nanocomposites, to 50 emu/g for NFC@Fe$_3$O$_4$@TNP nanocomposites. These results may be attributed to the reduced amount of magnetite core due to the addition of non-magnetic component (NFC and TNP). Yet, the relatively high saturation magnetization of 50 emu/g of

NFC@Fe$_3$O$_4$@TNP nanocomposites makes them tenable for recycling process by applying an external magnetic field [24].

The magnetic properties of NFC@Fe$_3$O$_4$@TNP nanocomposites after different cycles are shown in Fig. 10(b). It can be concluded that the magnetization value of NFC@Fe$_3$O$_4$@TNP nanocomposites had a marginal loss (from 50 to 45 emu/g) after fifteen cycles,

however, were still sufficient to induce stable superparamagnetic properties during the recycling process.

4. Conclusions

The nano-fibrillated cellulose/magnetite/titanium dioxide ($NFC@Fe_3O_4@TNP$) nanocomposites for photocatalytic hydrogen generation were successfully synthesized via the in-situ preparation of Fe_3O_4 NP and adsorption of TNP on the surface of NFC in a sequential order. It was found that NFC is a versatile support/carrier for both Fe_3O_4 NP and TNP, and that the $NFC@Fe_3O_4@TNP$ nanocomposites can significantly improve the photocatalytic efficiency and the recyclability of TNP. The TEM, XRD, XPS, FTIR and Raman spectra results showed that both Fe_3O_4 NP and TNP were uniformly loaded on the surface of NFC. Photocatalytic activity study showed that $NFC@Fe_3O_4@TNP$ nanocomposites had a higher photocatalytic hydrogen generation rate (436 μmol/(min gTNP)) in comparison with that of the NFC-TNP sample (272 μmol/(min gTNP)), and that $NFC@Fe_3O_4@TNP$ nanocomposites can be recycled with a marginal loss of photocatalytic efficiency after fifteen cycles. The results of this research suggest the potential of using cellulose nanomaterial as supports/carriers for both photocatalysts (such as TNP) and magnetite NP, to improve the photocatalytic efficiency and recyclability of the TNP-based nano-catalysts applications, such as waste water treatment and biomedical engineering.

Author contributions

The manuscript was written through contributions of all authors. All authors have given approval to the final version of the manuscript.

Notes

The authors declare no competing financial interest.

Acknowledgements

Appendix A. Supplementary data

Supplementary data associated with this article can be found, in the online version, at http://dx.doi.org/10.1016/j.apcatb.2017.01.021.

References

[1] A.F. Turbak, F.W., Snyder, K.R. Sandberg, Microfibrillated cellulose, a new cellulose product: properties, uses, and commercial potential, J. Appl. Polym. Sci.: Appl. Polym. Symp.;(United States), ITT Rayonier Inc., Shelton, WA, 1983.

[2] M.S. Jahan, A. Saeed, Z. He, Y. Ni, Jute as raw material for the preparation of microcrystalline cellulose, Cellulose 18 (2011) 451–459.

[3] X. An, Y. Wen, D. Cheng, X. Zhu, Y. Ni, Preparation of cellulose nano-crystals through a sequential process of cellulase pretreatment and acid hydrolysis, Cellulose 23 (2016) 2409–2420.

[4] M. Iguchi, S. Yamanaka, A. Budhiono, Bacterial cellulose—a masterpiece of nature's arts, J. Mater. Sci. 35 (2000) 261–270.

[5] K. Dimic-Misic, A. Puisto, P. Gane, K. Nieminen, M. Alava, J. Paltakari, T. Maloney, The role of MFC/NFC swelling in the rheological behavior and dewatering of high consistency furnishes, Cellulose 20 (2013) 2847–2861.

[6] Q. Li, S. McGinnis, C. Sydnor, A. Wong, S. Renneckar, Nanocellulose life cycle assessment, ACS Sustain. Chem. Eng. 1 (2013) 919–928.

[7] Y. Li, H. Zhu, F. Shen, J. Wan, S. Lacey, Z. Fang, H. Dai, L. Hu, Nanocellulose as green dispersant for two-dimensional energy materials, Nano Energy 13 (2015) 346–354.

[8] S. Li, J. Huang, Cellulose-rich nanofiber-based functional nanoarchitectures, Adv. Mater. 28 (2016) 1143–1158.

[9] H. Koga, E. Tokunaga, M. Hidaka, Y. Umemura, T. Saito, A. Isogai, T. Kitaoka, Topochemical synthesis and catalysis of metal nanoparticles exposed on crystalline cellulose nanofibers, Chem. Commun. 46 (2010) 8567–8569.

[10] X. An, Y. Wen, A. Almujil, D. Cheng, J. Li, X. Jia, J. Zou, Y. Ni, Nano-fibrillated cellulose (NFC) as versatile carriers of TiO_2 nanoparticles (TNPs) for photocatalytic hydrogen generation, RSC Adv. 6 (2016) 89457–89466.

[11] J. Puls, S.A. Wilson, D. Hölter, Degradation of cellulose acetate-based materials: a review, J. Polym. Environ. 19 (2010) 152–165.

[12] Y. Iguchi, H. Ichiura, T. Kitaoka, H. Tanaka, Preparation and characteristics of high performance paper containing titanium dioxide photocatalyst supported on inorganic fiber matrix, Chemosphere 53 (2003) 1193–1199.

[13] S. Bala, I. Mondal, A. Goswami, U. Pal, R. Mondal, Co-MOF as a sacrificial template: manifesting a new Co_3O_4/TiO_2 system with a p–n heterojunction for photocatalytic hydrogen evolution, J. Mater. Chem. A 3 (2015) 20288–20296.

[14] P.A. Bharad, K. Sivaranjani, C.S. Gopinath, A rational approach towards enhancing solar water splitting: a case study of Au-RGO/N-RGO-TiO_2, Nanoscale 7 (2015) 11206–11215.

[15] L. Chen, R.M. Berry, K.C. Tam, Synthesis of β-cyclodextrin-modified cellulose nanocrystals (CNCs)@Fe_3O_4@SiO_2 superparamagnetic nanorods, ACS Sustain. Chem. Eng. 2 (2014) 951–958.

[16] A. Maleki, M. Kamalzare, Fe_3O_4@cellulose composite nanocatalyst: preparation, characterization and application in the synthesis of benzodiazepines, Catal. Commun. 53 (2014) 67–71.

[17] K. Cheng, S. Peng, C. Xu, S. Sun, Porous hollow Fe_3O_4 nanoparticles for targeted delivery and controlled release of cisplatin, J. Am. Chem. Soc. 131 (2009) 10637–10644.

[18] J. Bao, W. Chen, T. Liu, Y. Zhu, P. Jin, L. Wang, J. Liu, Y. Wei, Y. Li, Bifunctional Au-Fe_3O_4 nanoparticles for protein separation, ACS Nano 1 (2007) 293–298.

[19] J.W. Xu, Z.D. Gao, K. Han, Y. Liu, Y.Y. Song, Synthesis of magnetically separable $Ag_3PO_4/TiO_2/Fe_3O_4$ heterostructure with enhanced photocatalytic performance under visible light for photoinactivation of bacteria, ACS Appl. Mater. Interfaces 6 (2014) 15122–15131.

[20] S. Challagulla, R. Nagarjuna, R. Ganesan, S. Roy, Acrylate-based polymerizable sol–gel synthesis of magnetically recoverable TiO_2 supported Fe_3O_4 for Cr(VI) photoreduction in aerobic atmosphere, ACS Sustain. Chem. Eng. 4 (2016) 974–982.

[21] X. Feng, H. Guo, K. Patel, H. Zhou, X. Lou, High performance, recoverable Fe_3O_4 ZnO nanoparticles for enhanced photocatalytic degradation of phenol, Chem. Eng. J. 244 (2014) 327–334.

[22] W.S. Tung, W.A. Daoud, New approach toward nanosized ferrous ferric oxide and Fe_3O_4-doped titanium dioxide photocatalysts, ACS Appl. Mater. Interfaces 1 (2009) 2453–2461.

[23] D. Chen, Y. Li, J. Zhang, J.-Z. Zhou, Y. Guo, H. Liu, Magnetic Fe_3O_4/ZnCr-layered double hydroxide composite with enhanced adsorption and photocatalytic activity, Chem. Eng. J. 185 (2012) 120–126.

[24] M. Abbas, B.P. Rao, V. Reddy, C. Kim, Fe_3O_4/TiO_2 core/shell nanocubes: single-batch surfactantless synthesis, characterization and efficient catalysts for methylene blue degradation, Ceram. Int. 40 (2014) 11177–11186.

[25] F. Ye, A. Ohmori, The photocatalytic activity and photo-absorption of plasma sprayed TiO_2-Fe_3O_4 binary oxide coatings, Surf. Coat. Technol. 160 (2002) 62–67.

[26] Q. He, Z. Zhang, J. Xiong, Y. Xiong, H. Xiao, A novel biomaterial-Fe_3O_4:TiO_2 core-shell nano particle with magnetic performance and high visible light photocatalytic activity, Opt. Mater. 31 (2008) 380–384.

[27] J. Safari, L. Javadian, Ultrasound assisted the green synthesis of 2-amino-4H-chromene derivatives catalyzed by Fe_3O_4-functionalized nanoparticles with chitosan as a novel and reusable magnetic catalyst, Ultrason. Sonochem. 22 (2015) 341–348.

[28] M. Răcuciu, D. Creangă, A. Airinei, Citric-acid-coated magnetite nanoparticles for biological applications, Eur. Phys. J. E 21 (2006) 117–121.

[29] H. Xu, J.S. Van Deventer, Microstructural characterisation of geopolymers synthesised from kaolinite/stilbite mixtures using XRD, MAS-NMR, SEM/EDX, TEM/EDX, and HREM, Cem. Concr. Res. 32 (2002) 1705–1716.

[30] R. Bardet, M.N. Belgacem, J. Bras, Different strategies for obtaining high opacity films of MFC with TiO_2 pigments, Cellulose 20 (2013) 3025–3037.

[31] H. Zhu, M. Fang, Z. Huang, Y. -g. Liu, K. Chen, C. Tang, M. Wang, L. Zhang, X. Wu, Novel carbon-incorporated porous $ZnFe_2O_4$ nanospheres for enhanced photocatalytic hydrogen generation under visible light irradiation, RSC Adv. 6 (2016) 56069–56076.

[32] Q. Han, B. Wang, J. Gao, Z. Cheng, Y. Zhao, Z. Zhang, L. Qu, Atomically thin mesoporous nanomesh of graphitic C_3N_4 for high-efficiency photocatalytic hydrogen evolution, ACS Nano 10 (2016) 2745–2751.

[33] P. Cheng, Z. Yang, H. Wang, W. Cheng, M. Chen, W. Shangguan, G. Ding, TiO_2–graphene nanocomposites for photocatalytic hydrogen production from splitting water, Int. J. Hydr. Energy 37 (2012) 2224–2230.

[34] S. Liu, M. Tamura, Y. Nakagawa, K. Tomishige, One-pot conversion of cellulose into n-Hexane over the Ir-ReO x/SiO_2 catalyst combined with HZSM-5, ACS Sustain. Chem. Eng. 2 (2014) 1819–1827.

[35] S. Liu, K. Yao, L.-H. Fu, M.-G. Ma, Selective synthesis of Fe_3O_4, γ-Fe_2O_3, and α-Fe_2O_3 using cellulose-based composites as precursors, RSC Adv. 6 (2016) 2135–2140.

[36] Y. Zhao, C. Tao, G. Xiao, G. Wei, L. Li, C. Liu, H. Su, Controlled synthesis and photocatalysis of sea urchin-like Fe_3O_4@TiO_2@Ag nanocomposites, Nanoscale 8 (2016) 5313–5326.

[37] K. Thamaphat, P. Limsuwan, B. Ngotaworncha, Phase characterization of TiO_2 powder by XRD and TEM, Kasetsart J. (Nat. Sci.) 42 (2008) 357–361.

[38] D. Sun, J. Yang, J. Li, J. Yu, X. Xu, X. Yang, Novel Pd-Cu/bacterial cellulose nanofibers: preparation and excellent performance in catalytic denitrification, Appl. Surf. Sci. 256 (2010) 2241–2244.

[39] R. Tanner, Y. Liang, E. Altman, Structure and chemical reactivity of adsorbed carboxylic acids on anatase TiO_2 (001), Surf. Sci. 506 (2002) 251–271.

[40] S. Ma, S. Zhan, Y. Jia, Q. Zhou, Superior antibacterial activity of Fe_3O_4-TiO_2 nanosheets under solar light, ACS Appl. Mater. Interfaces 7 (2015) 21875–21883.

[41] X.-L. Dong, X.-Y. Mou, H.-C. Ma, X.-X. Zhang, X.-F. Zhang, W.-J. Sun, C. Ma, M. Xue, Preparation of CdS-TiO_2/Fe_3O_4 photocatalyst and its photocatalytic properties, J. Sol-Gel Sci. Technol. 66 (2013) 231–237.

[42] M. Zaman, H. Xiao, F. Chibante, Y. Ni, Synthesis and characterization of cationically modified nanocrystalline cellulose, Carbohydr. Polym. 89 (2012) 163–170.

[43] B. Erdem, R.A. Hunsicker, G.W. Simmons, E.D. Sudol, V.L. Dimonie, M.S. El-Aasser, XPS and FTIR surface characterization of TiO_2 particles used in polymer encapsulation, Langmuir 17 (2001) 2664–2669.

[44] R. Sui, A.S. Rizkalla, P.A. Charpentier, FTIR study on the formation of TiO_2 nanostructures in supercritical CO_2, J. Phys. Chem. B 110 (2006) 16212–16218.

[45] C.-T. Chen, Y.-C. Chen, Fe_3O_4/TiO_2 core/shell nanoparticles as affinity probes for the analysis of phosphopeptides using TiO_2 surface-assisted laser desorption/ionization mass spectrometry, Anal. Chem. 77 (2005) 5912–5919.

[46] J.H. Wiley, R.H. Atalla, Band assignments in the Raman spectra of celluloses, Carbohydr. Res. 160 (1987) 113–129.

[47] M.J. Uddin, F. Cesano, F. Bonino, S. Bordiga, G. Spoto, D. Scarano, A. Zecchina, Photoactive TiO_2 films on cellulose fibres: synthesis and characterization, J. Photochem. Photobiol. A: Chem. 189 (2007) 286–294.

[48] T. Muraliganth, A.V. Murugan, A. Manthiram, Facile synthesis of carbon-decorated single-crystalline Fe_3O_4 nanowires and their application as high performance anode in lithium ion batteries, Chem. Commun. (2009) 7360–7362.

[49] T. Harifi, M. Montazer, A novel magnetic reusable nanocomposite with enhanced photocatalytic activities for dye degradation, Sep. Purif. Technol. 134 (2014) 210–219.

[50] S. Ren, R. Prakash, D. Wang, V.S.K. Chakravadhanula, M. Fichtner, Fe_3O_4 anchored onto helical carbon nanofibers as high-performance anode in lithium-ion batteries, ChemSusChem 5 (2012) 1397–1400.

[51] M. Mirjalili, Preparation of electroconductive, magnetic, antibacterial, and ultraviolet-blocking cotton fabric using reduced graphene oxide nanosheets and magnetite nanoparticles, Fibers Polym. 17 (2016) 1579–1588.

[52] K.A. Mahmoud, E. Lam, S. Hrapovic, J.H. Luong, Preparation of well-dispersed gold/magnetite nanoparticles embedded on cellulose nanocrystals for efficient immobilization of papain enzyme, ACS Appl. Mater. Interfaces 5 (2013) 4978–4985.